Electronic Supplementary Material (ESI) for Nanoscale.

This supplementary information was **updated** on **12/08/2020.**

Accurate modeling of a biological nanopore with an extended continuum framework

Due to an erroneous scaling factor, the values of the chloride mobility in Fig. S2c were plotted approximately 10 times larger than their true values, and this has now been corrected. The original version of Figure S2c, along with the unaltered caption, is displayed below for future reference. In addition, Equation S25 contained an error: the parameters d_{cis} and d_{trans} should have been 6 and 3.3 nm, respectively. These mistakes have now been corrected.

Please contact Nanoscale@rsc.org with any inquiries, citing the DOI: doi.org/10.1039/D0NR03114C

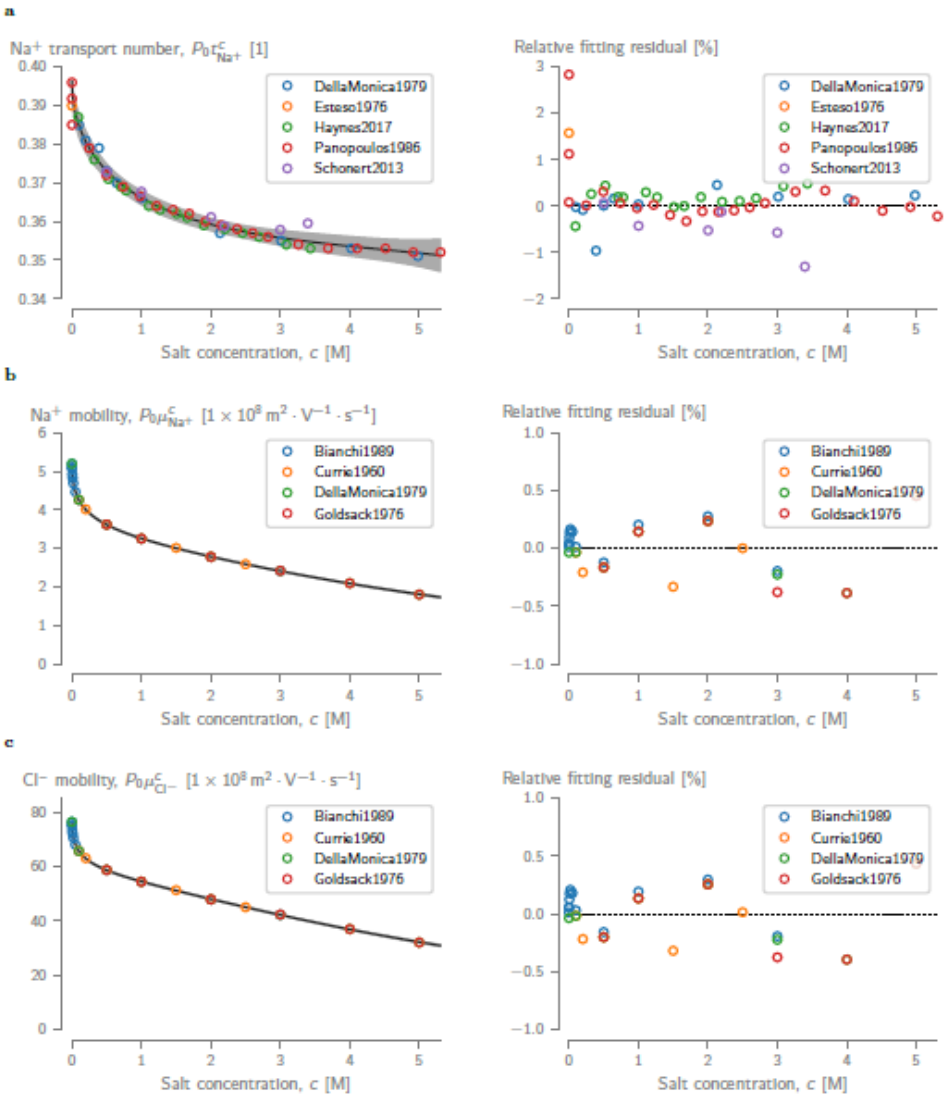

Figure S2. Concentration dependency of the cation transport number and the ion electrophoretic mobilities in NaCl. (a) Na^+ transport numbers and,[4–8] (b) Na^+ and (c) Cl^- electrophoretic mobilities[6,9–11] as a function of the bulk NaCl concentration (left) and the relative residuals after fitting (right) of Eq. (S1). Circles represent the experimental data and solid lines the fitted equation with the grey shading as the 3σ confidence interval.

Supporting Information:

Accurate modeling of a biological nanopore with an extended continuum framework

Kherim Willems,[†,‡] Dino Ruić,[¶,‡] Florian Lucas,[§] Ujjal Barman,[‡] Niels Verellen,[‡] Johan Hofkens,[†] Giovanni Maglia,[*,§] and Pol Van Dorpe[*,†,‡]

†*KU Leuven, Department of Chemistry, Celestijnenlaan 200F, B-3001 Leuven, Belgium*

‡*imec, Kapeldreef 75, B-3001 Leuven, Belgium*

¶*KU Leuven, Department of Physics and Astronomy, Celestijnenlaan 200D, B-3001 Leuven, Belgium*

§*University of Groningen, Groningen Biomolecular Sciences & Biotechnology Institute, 9747 AG, Groningen, The Netherlands*

E-mail: g.maglia@rug.nl; Pol.VanDorpe@imec.be

Contents

1 Extended materials and methods **S-3**

1.1 ClyA-AS mutations w.r.t. the wild-type S-3

1.2 Fitting of the concentration and wall distance functions to electrolyte data . S-3

1.2.1 Concentration-dependent fitting functions for bulk electrolyte data. . S-4

1.2.2 Wall distance-dependent fitting functions for molecular dynamics data. S-8

1.3 Surface integration to compute pore averaged values S-12

1.4 Weak forms of the ePNP-NS equations S-13

1.5 Estimating the bulk conductance of ClyA S-16

2 Extended results **S-18**

2.1 Effect of individual corrections to the ionic and water conductance S-18

2.1.1 Effect of disabling the wall distance corrections. S-18

2.1.2 Effect of disabling the concentration corrections. S-18

2.1.3 Effect of disabling the steric corrections. S-19

2.2 Tabulated ion selectivities S-20

2.3 Ionic current rectification S-21

2.4 Peak values of the radial potential profiles inside ClyA S-22

2.5 Comparison of the *lumen* diameters S-22

2.6 Per-residue B-factors of the molecular dynamics trajectory S-23

References **S-26**

1 Extended materials and methods

1.1 ClyA-AS mutations w.r.t. the wild-type

The mutations required to convert the wild-type *S. tyhpii* ClyA to the more widely used ClyA-AS are given in Tab. S1.[1]

Table S1. Mutations of the ClyA-AS variant compared to the *S. tyhpii* wild-type.

	Residue number													
Mutant	8	15	38	57	67	87	90	95	99	103	118	119	124	125
WT	Lys	Asn	Gln	Ala	Thr	Cys	Ala	Ala	Leu	Glu	Lys	Leu	Ile	Thr
AS	Gln	Ser	Lys	Glu	Val	Ala	Val	Ser	Gln	Gly	Arg	Ile	Val	Lys
Mutant	136	166	172	185	212	214	217	224	227	244	276	285	290	
WT	Val	Phe	Lys	Val	Lys	Lys	Ser	Thr	Asn	Thr	Glu	Cys	Lys	
AS	Thr	Tyr	Arg	Ile	Asn	Arg	Thr	Ser	Ala	Ala	Gly	Ser	Gln	

1.2 Fitting of the concentration and wall distance functions to electrolyte data

The properties of the ions and water molecules in the electrolyte depend strongly on the salt concentration (c) and the distance from the protein wall (d). To obtain reasonable estimates of these values for any given NaCl concentration or wall distance, we fitted a series of empirical polynomial functions (using non-linear regression with the 'lmfit' Python package[2]) to literature data—either bulk electrolyte experimental data for the concentration dependencies and molecular dynamics data for the wall distance dependencies. We fitted equations to concentration data for the ion self-diffusion coefficients ($\mathcal{D}_i^c(c)$, Eq. (S1) and Figs. S1a and S1b), the ion electrophoretic mobilities ($\mu_i^c(c)$, Eq. (S1) and Fig. S2b), and the cation transport number ($t^c_{\mathrm{Na}^+}(c)$, Eq. (S1) and Fig. S2a), the electrolyte viscosity ($\eta^c(c)$, Eq. (S2) and Fig. S3a), the electrolyte density ($\varrho^c(c)$, Eq. (S3) and Fig. S3b) and the electrolyte relative permittivity ($\varepsilon^c_{r,\mathrm{f}}(c)$, Eq. (S4) and Fig. S3c). Wall distance parameters were determined

for ion self-diffusion coefficients ($\mathcal{D}_i^w(d)$, Eq. (S5) and Fig. S4a), the ion electrophoretic mobilities ($\mu_i^w(d)$, Eq. (S5) and Fig. S4a), and the electrolyte viscosity ($\eta^w(d)$, Eq. (S6) and Fig. S4b). All best-fit parameters can be found in Tab. S2, and the fitting functions are described below.

1.2.1 Concentration-dependent fitting functions for bulk electrolyte data.

Diffusivity, mobility and transport number. The NaCl concentration dependency data of ion self-diffusion coefficients, the ion electrophoretic mobilities and the cation trans-

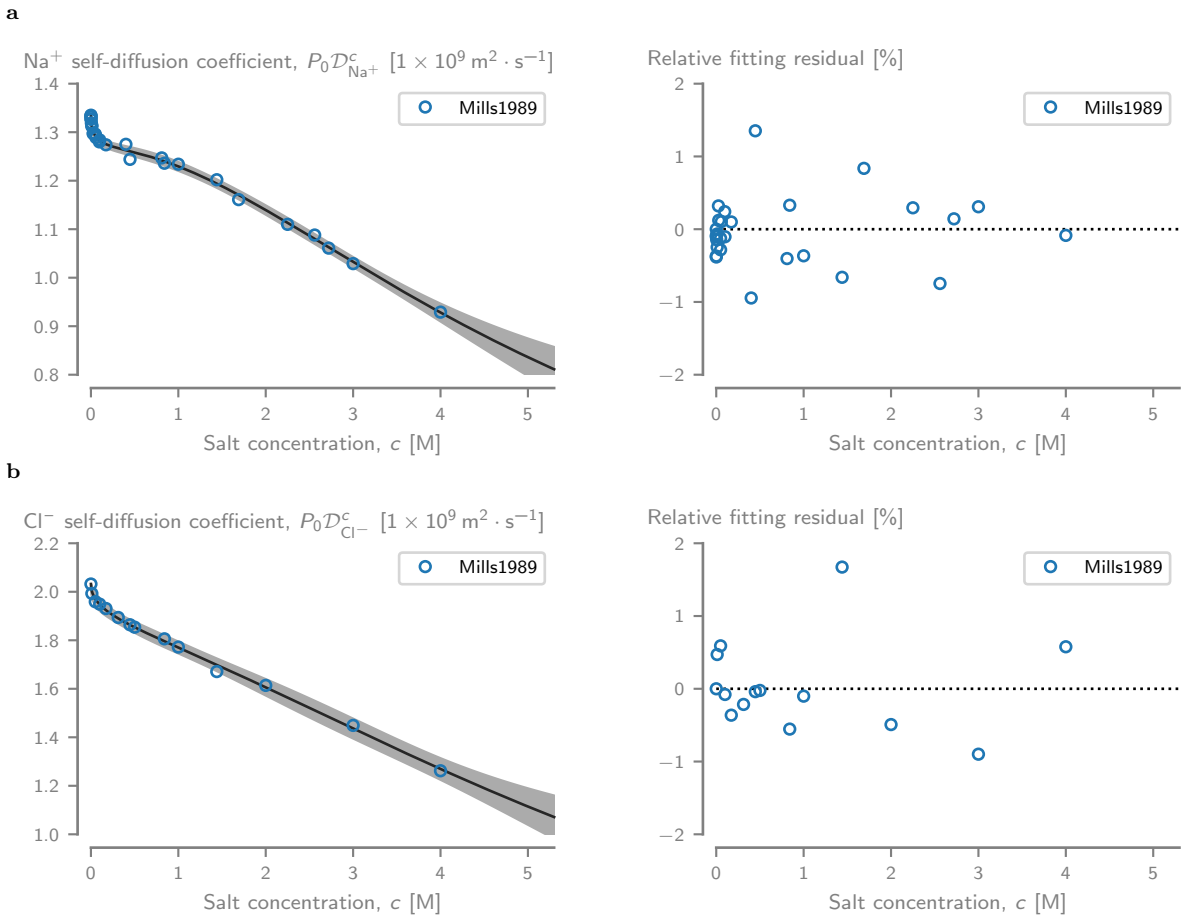

Figure S1. Concentration dependency of ion self-diffusion coefficients in NaCl. (a) Na^+ and (b) Cl^- self-diffusion coefficients[3] as a function of the bulk NaCl concentration (left) and the relative residuals after fitting (right) of Eq. (S1). Circles represent the experimental data and solid lines the fitted equation with the grey shading as the 3σ confidence interval.

port number were fitted to

$$X_i(c) = P_0 X_i^c(c) = P_0 \left[1 + P_1 c^{0.5} + P_2 c + P_3 c^{1.5} + P_4 c^2\right]^{-1} \tag{S1}$$

with X either $\mathcal{D}$ (diffusion), μ (mobility) or t (transport number) and i either Na^+ or Cl^-. P_0 is the value at infinite dilution (*i.e.*, $c = 0\,\mathrm{M}$) and fixed during fitting of parameters P_1, P_2, P_3 and P_4.

Viscosity. The concentration dependency of the electrolyte viscosity was fitted to

$$\eta(c) = P_0 \eta^c(c) = P_0 \left[1 + P_1 c^{0.5} + P_2 c + P_3 c^2 + P_4 c^{3.5}\right] \tag{S2}$$

with P_0 the value at infinite dilution.

Density. The concentration dependency of the electrolyte density was fitted to

$$\varrho(c) = P_0 \varrho^c(c) = P_0 \left[1 + P_1 c + P_2 c^2\right] \tag{S3}$$

with P_0 the value at infinite dilution.

Relative permittivity. For the concentration dependency of the electrolyte relative permittivity, we used the microfield model developed by Gavish *et al.*[12]

$$\varepsilon_r(c) = P_0 \varepsilon_{r,\mathrm{f}}^c(c) = P_0 \left[1 - \left(1 - \frac{P_1}{P_0}\right) L\left(\frac{3P_2}{P_0 - P_1} c\right)\right] \tag{S4}$$

where L is the Langevin function ($L(x) = \coth(x) - 1/x$), P_0 the value at infinite dilution, P_1 the limiting permittivity ($\varepsilon_{r,ms}$) and P_2 the total excess polarization of the ions (α). Even though we fitted the equation to our literature dataset[13] ($P_1 = 29.50 \pm 1.32$ and $P_2 = 11.74 \pm 0.21$), we opted to make use of the parameters given by Gavish for NaCl at 298.15 K ($P_1 = 30.08$ and $P_2 = 11.5$).[12]

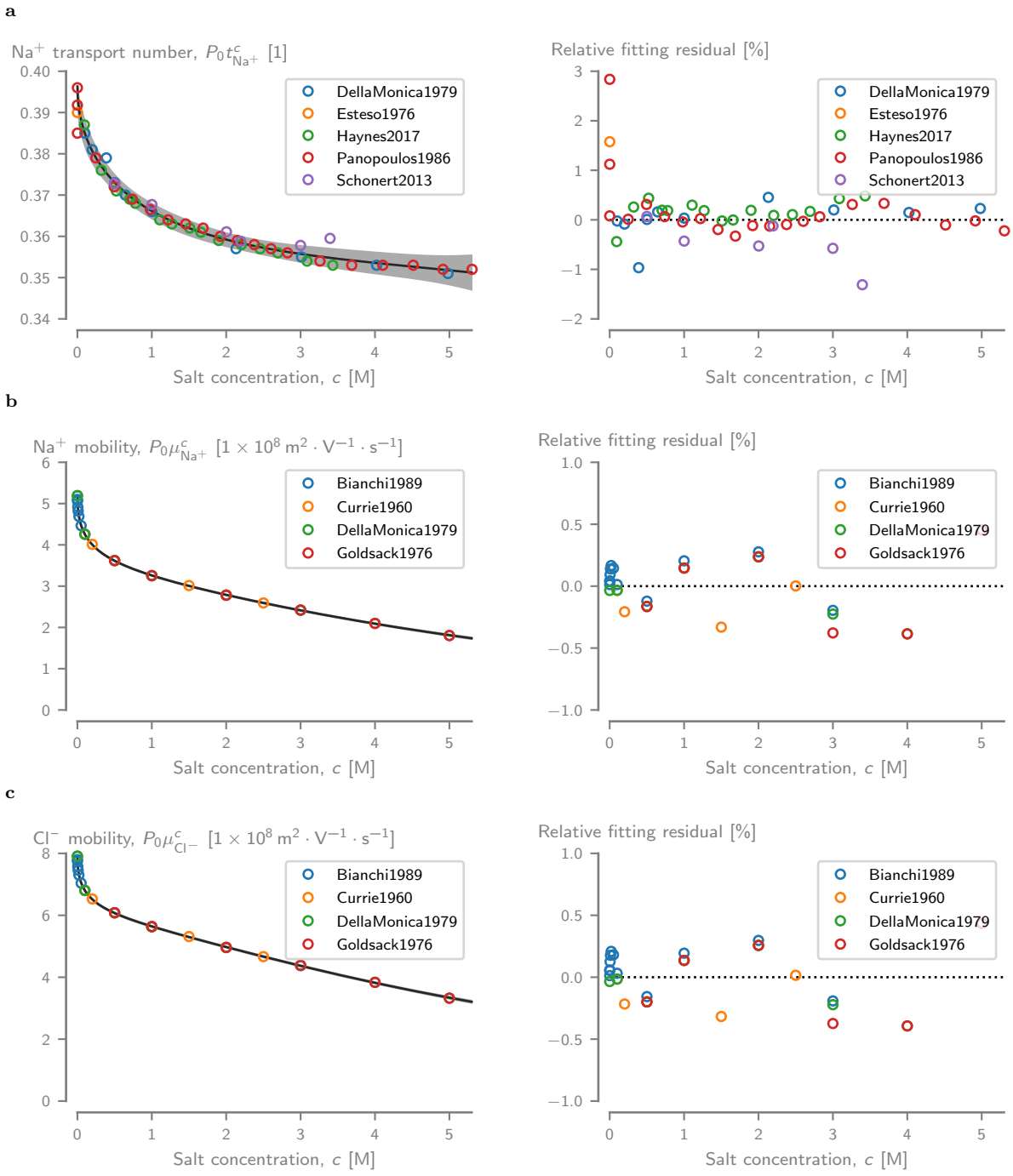

Figure S2. Concentration dependency of the cation transport number and the ion electrophoretic mobilities in NaCl. (a) Na^+ transport numbers and,[4–8] (b) Na^+ and (c) Cl^- electrophoretic mobilities[6,9–11] as a function of the bulk NaCl concentration (left) and the relative residuals after fitting (right) of Eq. (S1). Circles represent the experimental data and solid lines the fitted equation with the grey shading as the 3σ confidence interval.

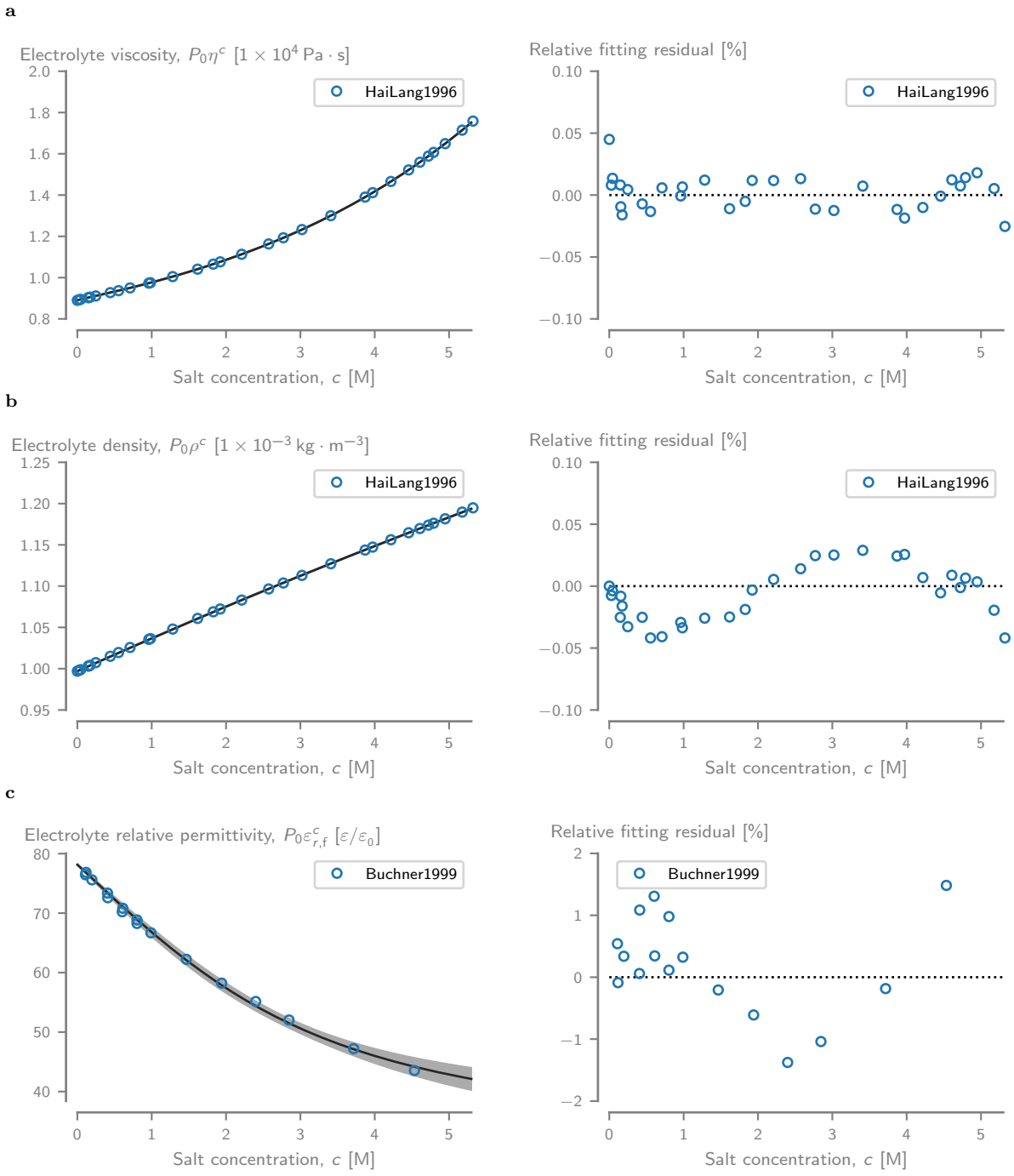

Figure S3. Concentration dependency of the electrolyte viscosity, density and relative permittivity in NaCl. (a) Viscosity,[14] (b) density[14] and (c) relative permittivity[12,13] as a function of the bulk NaCl concentration (left) and the relative residuals after fitting (right) to Eqs. (S2), (S3) and (S4), respectively. Circles represent the experimental data and solid lines the fitted equation with the grey shading as the 3σ confidence interval.

1.2.2 Wall distance-dependent fitting functions for molecular dynamics data.

Diffusivity and mobility. The protein wall distance function used for the ion self-diffusion coefficients and the ion electrophoretic mobilities was taken from Simakov *et al.*[15], who fitted it to the molecular dynamics data from Makarov *et al.*[16]. The function is a sigmoidal given by

$$X_i^w(d) = 1 - \exp -P_1(d - P_2) \tag{S5}$$

with X either $\mathcal{D}$ (diffusion) or μ (mobility) and i either Na^+ or Cl^- and P_1 (a) and P_2 (r_0) the fitting parameters. For P_1, we used the value determined by Simakov ($6.2\,\mathrm{nm}^{-1}$), but for P_2 we opted to use a value of 0.01 nm instead of 0.22 nm proposed by Simakov[15] and futher corroborated by Wilson *et al.*.[17] We chose this smaller offset because Eq. (S5) quickly becomes negative beyond the offet P_2, resulting in unphysical values. Pederson *et al.* solved this by setting an arbitrary mininum positive value for the diffusion coefficient,[18] but this would result in a 'dead' zone of nearly 0.2 nm from each wall with a very low diffusivity (several orders of magnitude below the bulk value). This would make the current of a pore with a diameter smaller than 0.5 nm effectively zero, which has been shown experimentally to be not the case.[19] In addition, P_2 represents the center-to-center distance between the ion and the nearest heavy atom, meaning that approximately half of the 0.22 nm would already be inside our geometry (*i.e.*, within the van der Waals radius of the heavy atom), and the other half would be inaccessible to ions due to excluded volume effects. As we are not modelling the latter, we opted to assign the full offset given by P_2 to the heavy atom, effectively assuming that all ion-inaccessible space is taken into account already by our geometry. Our choice of parameters leads to a values of $X_i^w(0\,\mathrm{nm}) = 0.06$ (*i.e.*, at the wall boundary) and $X_i^w(0.75\,\mathrm{nm}) = 0.99$ (*i.e.*, 0.75 nm within the electrolyte, Fig. S4a), which roughly corresponds to the values reported by Wilson *et al.*.[17]

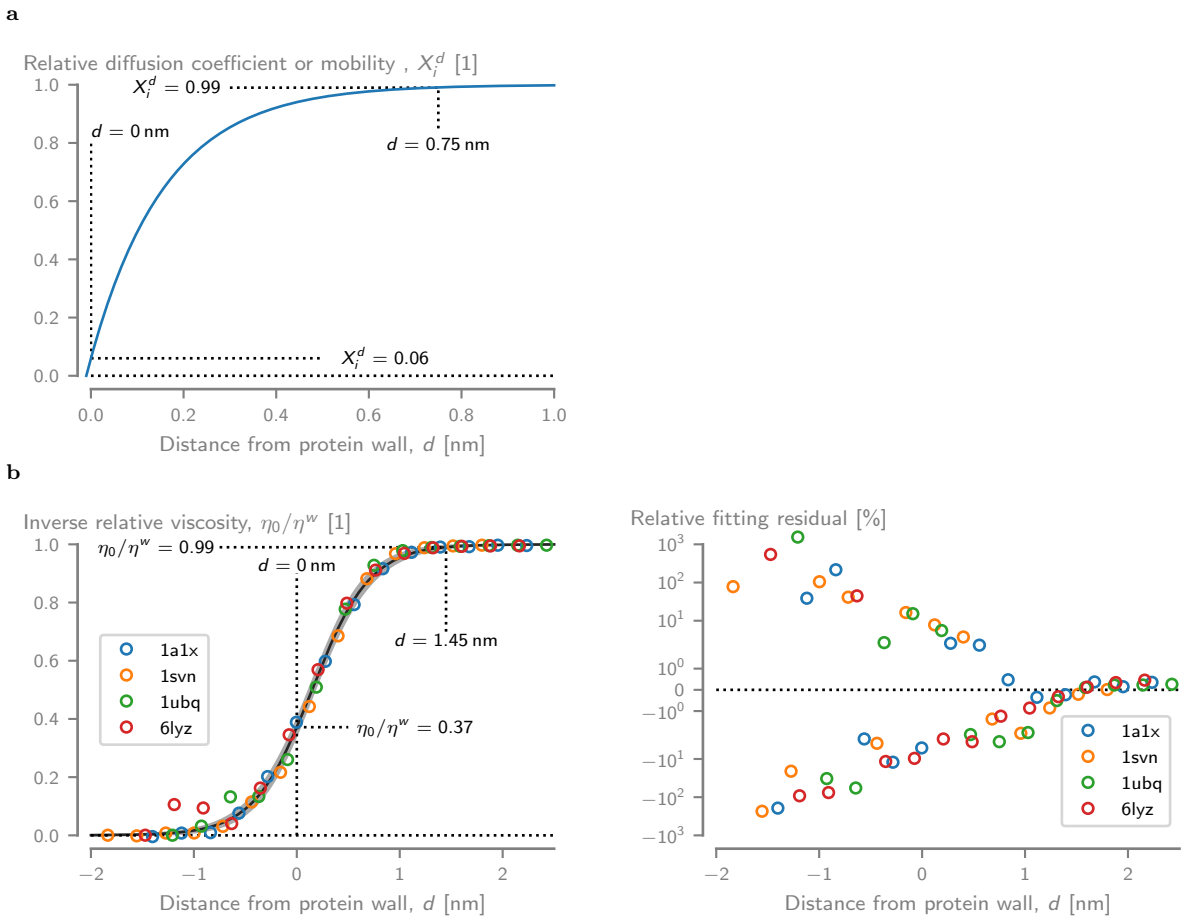

Figure S4. Wall distance dependency of ion self-diffusion coefficients, mobilities and electrolyte viscosity. (a) Relative ion self-diffusion coefficient and mobility,[15–18] and (b) inverse relative viscosity[20] as a function of the distance from the protein wall (left) and the relative residuals after fitting (right) to Eqs. (S5) and (S6), respectively. Circles represent the experimental data and solid lines the fitted equation with the grey shading as the 3σ confidence interval.

Viscosity. Analogously to the diffusivity of ions, the movement of water molecules near a protein wall is also hampered,[16] resulting in substantially higher viscosities.[20] To model this, we fitted the following logistic curve to the molecular dynamics data from Pronk *et al.*[20]

$$\eta^w(d) = 1 + \exp\left(-P_1(d - P_2)\right) \tag{S6}$$

with P_1 and P_2 the fitting parameters, representing the slope of the sigmoidal and the offset of the sigmoid's center from 0, respectively. Prior to the fitting, the viscosity data for all proteins was offset using by hydrodynamic radius, such that $d = 0\,\text{nm}$ represents

the mean distance from the wall for each protein, regardless of its size. Additionally, we normalized and inverted the relative viscosities (η_0/η^w) allowing us to fit values between 0 and 1. Our parameters result in a values of $\eta_0/\eta^w(0\,\mathrm{nm}) = 0.37$ (*i.e.*, at the protein wall) and $\eta_0/\eta^w(1.45\,\mathrm{nm}) = 0.99$ (*i.e.*, 1.45 nm within the electrolyte, Fig. S4b).

Table S2. Overview of the NaCl fitting parameters used for interpolation.

		Infinite dilution value		Fitting parameters					
Property	Eq.	P_0	Unit	P_1	P_2	P_3	P_4	R^2	References
$\mathcal{D}^c_{\mathrm{Na^+}}(c)$	Eq. (S1)	1.334	$1\times10^{-9}\,\mathrm{m^2\cdot s^{-1}}$	$2.02\pm0.14\times10^{-1}$	$-3.05\pm0.41\times10^{-1}$	$2.19\pm0.38\times10^{-1}$	$-3.13\pm1.08\times10^{-2}$	>0.99	3
$\mathcal{D}^c_{\mathrm{Cl^-}}(c)$	Eq. (S1)	2.032	$1\times10^{-9}\,\mathrm{m^2\cdot s^{-1}}$	$1.49\pm0.30\times10^{-1}$	$-4.94\pm9.04\times10^{-2}$	$3.40\pm8.26\times10^{-2}$	$1.43\pm2.30\times10^{-2}$	>0.99	3
$t^c_{\mathrm{Na^+}}(c)$	Eq. (S1)	0.3963	n.a.	$9.38\pm1.64\times10^{-2}$	$2.86\pm3.24\times10^{-3}$	$-1.88\pm6.52\times10^{-2}$	$4.51\pm2.75\times10^{-3}$	0.98	4–8
$\mu^c_{\mathrm{Na^+}}(c)$	Eq. (S1)	5.192	$1\times10^{-8}\,\mathrm{m^2\cdot s^{-1}\cdot V^{-1}}$	$7.91\pm0.06\times10^{-1}$	$-3.53\pm0.17\times10^{-1}$	$1.46\pm0.15\times10^{-1}$	$9.23\pm3.89\times10^{-3}$	>0.99	6,9–11
$\mu^c_{\mathrm{Cl^-}}(c)$	Eq. (S1)	7.909	$1\times10^{-8}\,\mathrm{m^2\cdot s^{-1}\cdot V^{-1}}$	$6.29\pm0.06\times10^{-1}$	$-4.29\pm0.17\times10^{-1}$	$2.12\pm0.14\times10^{-1}$	$-1.07\pm0.37\times10^{-2}$	>0.99	6,9–11
$\eta^c(c)$	Eq. (S2)	0.8904	$1\times10^{-4}\,\mathrm{Pa\cdot s}$	$7.56\pm0.27\times10^{-3}$	$7.77\pm0.04\times10^{-2}$	$1.19\pm0.01\times10^{-2}$	$5.95\pm0.35\times10^{-4}$	>0.99	14
$\varrho^c(c)$	Eq. (S3)	0.997	$1\times10^{3}\,\mathrm{kg\cdot m^{-3}}$	$4.06\pm0.01\times10^{-2}$	$-6.39\pm0.16\times10^{-4}$			>0.99	14
$\varepsilon^c_{r,\mathrm{f}}(c)$	Eq. (S4)	78.15	n.a.	$3.08\pm0.00\times10^{1}$	$1.15\pm0.00\times10^{1}$				12,13
$\mathcal{D}^w_i(d)$	Eq. (S5)			6.2	0.01				15,16,18
$\mu^w_i(d)$	Eq. (S5)			6.2	0.01				15,16,18
$\eta^w(d)$	Eq. (S6)			3.36 ± 0.23	$1.47\pm0.23\times10^{-1}$			0.97	20

1.3 Surface integration to compute pore averaged values

The average pore values for quantity of interest X was computed by Eq. (S7)

$$\langle X \rangle_\alpha = \frac{\iint_{V_\alpha} \beta_\alpha X \, dr \, dz}{\iint_{V_\alpha} \beta_\alpha \, dr \, dz} \, , \tag{S7}$$

where

$$\alpha = \begin{cases} \text{PT}, & d \geq 0 \text{ nm, average over the entire pore} \\ \text{PB}, & d > 0.5 \text{ nm, average over the pore 'bulk'} \\ \text{PS}, & d \leq 0.5 \text{ nm, average over the pore 'surface'} \end{cases} \tag{S8}$$

and

$$\beta_{\text{PT}} = \begin{cases} 1, & \text{if } -1.85 \leq z \leq 12.25 \text{ and } r \leq r_{\text{p}}(z) \\ 0, & \text{otherwise} \end{cases} \tag{S9}$$

$$\beta_{\text{PB}} = \begin{cases} 1, & \text{if } -1.85 \leq z \leq 12.25 \text{ and } r \leq r_{\text{p}}(z) \text{ and } d > 0.5 \\ 0, & \text{otherwise} \end{cases} \tag{S10}$$

$$\beta_{\text{PS}} = \begin{cases} 1, & \text{if } -1.85 \leq z \leq 12.25 \text{ and } r \leq r_{\text{p}}(z) \text{ and } d \leq 0.5 \\ 0, & \text{otherwise} \end{cases} \tag{S11}$$

with d the distance from the nanopore wall and $r_{\text{p}}(z)$ is the radius of the pore at height z.

1.4 Weak forms of the ePNP-NS equations

To solve partial differential equations with the finite element method, we must be derive their weak form. This is achieved through multiplication of the equation with an arbitrary test function and integration over their relevant domains and boundaries (Fig. S5). The full computational domain of our model (Ω) is subdivided into domains for the pore (Ω_p), the lipid bilayer (Ω_m) and the electrolyte reservoir (Ω_w). The relevant boundaries of these domains are also indicated, i.e. the reservoir's exterior edges at the *cis* $\Gamma_{w,c}$) and *trans* $\Gamma_{w,t}$) sides, the outer edge of the lipid bilayer (Γ_m) and the interface of the fluid with the nanopore and the bilayer (Γ_{p+m}).

The following paragraphs detail the equations that were used in this paper, together with their corresponding weak forms.

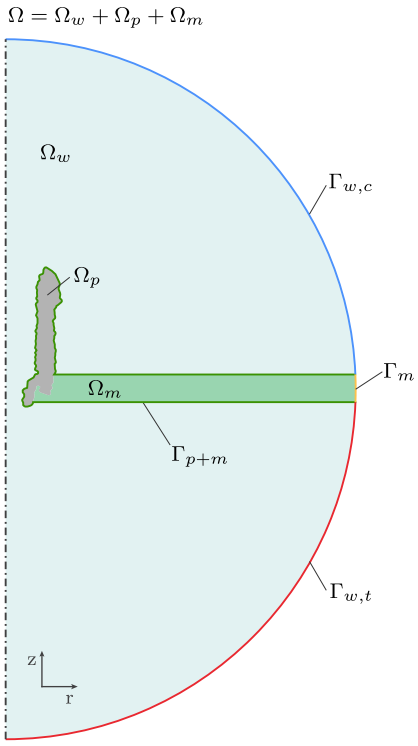

Figure S5. Computational domains and boundaries. The full computational domain (Ω) of the model is subdivided into various subdomains (Ω_x) and their limiting boundaries (Γ_x).

Poisson equation. The global potential distribution is described by the Poisson equation (PE)[21]

$$\nabla \cdot \boldsymbol{D} = -\left(\rho^{f}_{\text{pore}} + \rho_{\text{ion}}\right) \quad \text{with } \boldsymbol{D} = \varepsilon_0 \varepsilon_r \nabla\varphi \ , \tag{S12}$$

with $\boldsymbol{D}$ the electrical displacement field, φ the electric potential, ε_0 the vacuum permittivity ($8.854\,19{\times}10^{-12}\,\mathrm{F\,m^{-1}}$), and ε_r the local relative permittivity of the medium. ρ^{f}_{pore} and ρ_{ion} are the fixed (due to the pore) and mobile (due to the ions) charge distributions, respectively.

Multiplication of Eq. (S12) with the potential test function ψ and integration over the entire model $\Omega = \Omega_w + \Omega_p + \Omega_m$ gives

$$\int_{\Omega} \left[\nabla \cdot \boldsymbol{D}\right] \psi \, d\Omega = \ -\int_{\Omega} \left[\rho^{f}_{\text{pore}} + \rho_{\text{ion}}\right] \psi \, d\Omega \ , \tag{S13}$$

which, after applying the Gauss divergence theorem, yields the final weak formulation

$$\int_{\Omega} \left[\nabla\psi \cdot \boldsymbol{D}\right] \, d\Omega - \int_{\Gamma_{\text{PE}}} \left[\psi \boldsymbol{D} \cdot \boldsymbol{n}\right] \, d\Gamma_{\text{PE}} = \int_{\Omega} \left[\psi \rho^{f}_{\text{pore}}\right] \, d\Omega + \int_{\Omega} \left[\psi \rho_{\text{ion}}\right] \, d\Omega \ , \tag{S14}$$

with boundaries $\Gamma_{\text{PE}} = \Gamma_{w,c} + \Gamma_{w,t} + \Gamma_m$ and $\boldsymbol{n}$ their normal vector. The boundary integrals at $\Gamma_{w,c}$ and $\Gamma_{w,t}$ are evaluated using the Dirichlet boundary conditions (BCs) $\varphi = 0$ and $\varphi = V_{\text{b}}$, respectively. A zero charge BC, $\boldsymbol{n} \cdot \boldsymbol{D} = 0$, is used for the integral at Γ_m.

Size-modified Nernst-Planck equation. The total ionic flux $\boldsymbol{J}_i$ of ion i at steady-state is expressed by the size-modified Nernst-Planck equation (smNPE)[21]

$$\frac{\partial c_i}{\partial t} = -\nabla \cdot \boldsymbol{J}_i = -\nabla \cdot \left(\mathcal{D}_i \nabla c_i + z_i \mu_i c_i \nabla\varphi + \mathcal{D}_i \boldsymbol{\beta_i} c_i - \boldsymbol{u} c_i\right) \ , \tag{S15}$$

where

$$\boldsymbol{\beta_i} = \frac{a_i^3/a_0^3 \sum_j N_\mathrm{A} a_j^3 \nabla c_j}{1 - \sum_j N_\mathrm{A} a_j^3 c_j} \ , \tag{S16}$$

and with ion diffusion coefficient $\mathcal{D}_i$, concentration c_i, charge number z_i, mobility μ_i, electrostatic potential φ, steric saturation factor β_i and fluid velocity $\boldsymbol{u}$. N_A is Avogadro's constant ($6.022\times10^{23}\,\mathrm{mol}^{-1}$) and a_i and a_0 are the limiting cubic diameters for ions and water, respectively. Using the ion concentration test function d_i, the weak form of Eq. (S15) becomes

$$\begin{aligned}
\int_{\Omega_w} \left[\frac{\partial c_i}{\partial t}\right] d_i \, d\Omega_w &= \int_{\Omega_w} \left[-\nabla \cdot \boldsymbol{J}_i\right] d_i \, d\Omega_w \\
\int_{\Omega_w} \left[d_i \frac{\partial c_i}{\partial t}\right] \, d\Omega_w &= \int_{\Omega_w} \left[\nabla d_i \cdot \boldsymbol{J}_i\right] \, d\Omega_w - \int_{\Gamma_\mathrm{NP}} \left[d_i \boldsymbol{J}_i \cdot \boldsymbol{n}\right] \, d\Gamma_\mathrm{NP} \\
&= \int_{\Omega_w} \left[\nabla d_i \cdot \left(\mathcal{D}_i \nabla c_i + z_i \mu_i c_i \nabla \varphi + \mathcal{D}_i \boldsymbol{\beta_i} c_i - \boldsymbol{u} c_i\right)\right] \, d\Omega_w \\
&\quad - \int_{\Gamma_\mathrm{NP}} \left[d_i \left(\mathcal{D}_i \nabla c_i + z_i \mu_i c_i \nabla \varphi + \mathcal{D}_i \boldsymbol{\beta_i} c_i - \boldsymbol{u} c_i\right) \cdot \boldsymbol{n}\right] \, d\Gamma_\mathrm{NP} \ .
\end{aligned} \tag{S17}$$

The integrals on the boundaries $\Gamma_\mathrm{NP} = \Gamma_{w,c} + \Gamma_{w,t} + \Gamma_{p+m}$ are evaluated using the Dirichlet boundary condition $c_i = c_\mathrm{s}$ for $\Gamma_{w,c}$ and $\Gamma_{w,t}$, and the no flux boundary condition $\boldsymbol{n} \cdot \boldsymbol{J}_i = 0$ for Γ_{p+m}

Variable density and viscosity Navier-Stokes equation. The steady-state, laminar fluid flow of an incompressible fluid with a variable density and viscosity is given by the system of equations[22]

$$\boldsymbol{u} \cdot \nabla \varrho = 0 \tag{S18}$$

$$(\boldsymbol{u} \cdot \nabla)(\varrho \boldsymbol{u}) + \nabla \cdot \sigma_{ij} = \boldsymbol{F}_\mathrm{ion} \quad \text{with } \sigma_{ij} = p\mathbf{I} - \eta \left[\nabla \boldsymbol{u} + (\nabla \boldsymbol{u})^\mathsf{T}\right] \tag{S19}$$

$$\nabla \cdot (\varrho \boldsymbol{u}) - \boldsymbol{u} \cdot \nabla \varrho = 0 \ , \tag{S20}$$

with fluid velocity $\boldsymbol{u}$, density ϱ, hydrodynamic stress tensor σ_{ij}, viscosity η, pressure p and body force $\boldsymbol{F}_{\text{ion}}$. The pressure test function q is used to derive the weak forms of Eq. (S18)

$$\int_{\Omega_w} [\boldsymbol{u} \cdot \nabla \varrho]\, q\, d\Omega_w = \int_{\Omega_w} [q\boldsymbol{u} \cdot \nabla \varrho]\; d\Omega_w = 0 \;, \tag{S21}$$

and Eq. (S20)

$$\begin{aligned}\int_{\Omega_w} [\nabla \cdot (\varrho \boldsymbol{u}) - \boldsymbol{u} \cdot \nabla \varrho]\, q\, d\Omega_w &= \int_{\Omega_w} [\nabla \cdot (\varrho \boldsymbol{u})]\, q\, d\Omega_w - \int_{\Omega_w} [q\boldsymbol{u} \cdot \nabla \varrho]\; d\Omega_w \\ &= \int_{\Omega_w} [\nabla q \cdot (\varrho \boldsymbol{u})]\; d\Omega_w - \int_{\Gamma_{\text{NS}}} [q\,(\varrho \boldsymbol{u}) \cdot \boldsymbol{n}]\; d\Gamma_{\text{NS}} \\ &\quad - \int_{\Omega_w} [q\boldsymbol{u} \cdot \nabla \varrho]\; d\Omega_w \;,\end{aligned} \tag{S22}$$

while for Eq. (S19) we use the velocity test function $\boldsymbol{v} = [v_r, v_\phi, v_z]$

$$\begin{aligned}\int_{\Omega_w} [(\boldsymbol{u} \cdot \nabla)\,(\varrho \boldsymbol{u}) + \nabla \cdot \sigma_{ij}] \cdot \boldsymbol{v}\, d\Omega_w &= \int_{\Omega_w} \boldsymbol{F} \cdot \boldsymbol{v}\, d\Omega_w \\ \int_{\Omega_w} [(\boldsymbol{u} \cdot \nabla)\,(\varrho \boldsymbol{u}) \cdot \boldsymbol{v}]\; d\Omega_w & \\ - \int_{\Omega_w} [\sigma_{ij} \cdot \nabla \boldsymbol{v}]\; d\Omega_w + \int_{\Gamma_{\text{NS}}} [\boldsymbol{v} \cdot \sigma_{ij} \cdot \boldsymbol{n}]\; d\Gamma_{\text{NS}} &= \int_{\Omega_w} \boldsymbol{F} \cdot \boldsymbol{v}\, d\Omega_w \;,\end{aligned} \tag{S23}$$

with boundaries $\Gamma_{\text{NS}} = \Gamma_{w,c} + \Gamma_{w,t} + \Gamma_{p+m}$. The no-slip Dirichlet BC $\boldsymbol{u} = 0$ is applied to Γ_{p+m}, and the no normal stress $\sigma_{ij}\boldsymbol{n} = 0$ is used for $\Gamma_{w,c}$ and $\Gamma_{w,t}$.

1.5 Estimating the bulk conductance of ClyA

The ionic current flowing through a nanopore can be estimated using Ohm's law

$$I(c_{\text{s}}, V_{\text{b}}) = G_{\text{bulk}}(c_{\text{s}}) V_{\text{b}} \tag{S24}$$

with G_{bulk} the nanopore conductance and V_{b} the applied voltage. A naive estimate of G_{bulk} can be obtained by modelling it as a fluidic resistor, represented by a fluid-filled cylinder.[23]

Because ClyA has an asymmetric shape, it is best approximated by two resistors in series: a tall, wide cylinder (*cis lumen*) on top of a narrow short cylinder (*trans* constriction).[1] Hence,

$$G_{\mathrm{bulk}}(c_{\mathrm{s}}) = \frac{\sigma(c_{\mathrm{s}})\pi}{4}\left(\frac{l_{\mathrm{cis}}}{d_{\mathrm{cis}}^2} + \frac{l_{\mathrm{trans}}}{d_{\mathrm{trans}}^2}\right)^{-1}, \tag{S25}$$

with σ the (concentration dependent) bulk electrolyte conductivity. The *cis* and *trans* chambers have have heights and diameters of $l_{\mathrm{cis}} = 10\,\mathrm{nm}$ and $l_{\mathrm{trans}} = 4\,\mathrm{nm}$, and $d_{\mathrm{cis}} = 6\,\mathrm{nm}$ and $d_{\mathrm{trans}} = 3.3\,\mathrm{nm}$, respectively.[1]

2 Extended results

2.1 Effect of individual corrections to the ionic and water conductance

To estimate the influence to which each group of corrections (*i.e.*, the wall distance, concentration and steric effects) on the conductance properties of ClyA, we performed a set of simulations for the following conditions: ePNP-NS without wall distance corrections ($\mathcal{D}_i^w = 1$, $\mu_i^w = 1$, $\eta^w = 1$), ePNP-NS without concentration-dependent corrections ($\varepsilon_{r,\mathrm{f}}^c = 1$, $\mathcal{D}_i^c = 1$, $\mu_i^c = 1$, $\eta^c = 1$, $\varrho^c = 1$), ePNP-NS without steric effect ($\boldsymbol{\beta} = 0$). For comparison, we plotted the relative ionic conductance (Fig. S6a) and the relative water conductance (Fig. S6b) of these models, normalized over the values obtained with the full ePNP-NS equations.

2.1.1 Effect of disabling the wall distance corrections.

Disabling the wall distance corrections yields a higher (≈10 % increase) ionic conductance compared to the full ePNP-NS equations (Fig. S6a, blue curve). In effect, the implementation of the wall distance corrections results in an smaller effective pore size. The influence on the water flow is stronger, with the reduction of the viscosity near the wall giving rise to a 25 % to 50 % increase in the water flow (Fig. S6b, blue curve).

2.1.2 Effect of disabling the concentration corrections.

The removal of the concentration-dependent corrections has a large influence on the simulated results. The ionic conductance increases dramatically: from 5 %, 13 %, 29 % and 152 % at 0.005 M, 0.05 M, 0.5 M and 5 M, respectively (Fig. S6a, red curve). This is expected however, given that the large reduction of both diffusion coefficients and ionic mobilities with increasing salt concentrations is not taken into account. The influence on the water flow shows only a limited effect from 0.005 M (9 % decrease) to 1 M (2 % increase), followed by a rapid increase of 82 % between 1 M and 5 M (Fig. S6b, red curve). This is a direct

result of the 15 % increase of the electrolyte viscosity between 1 M to 5 M, compared to the mere 5 % increase between 0 M to 1 M (Fig. S3a).

2.1.3 Effect of disabling the steric corrections.

The steric corrections appear to have little influence on the ionic conductance, with a maximum deviation of at most ±3 % over the entire concentration range (Fig. S6a, brown curve). The effect on the water flow is larger, with a decrease of 10 % at 0.5 M (Fig. S6b, brown

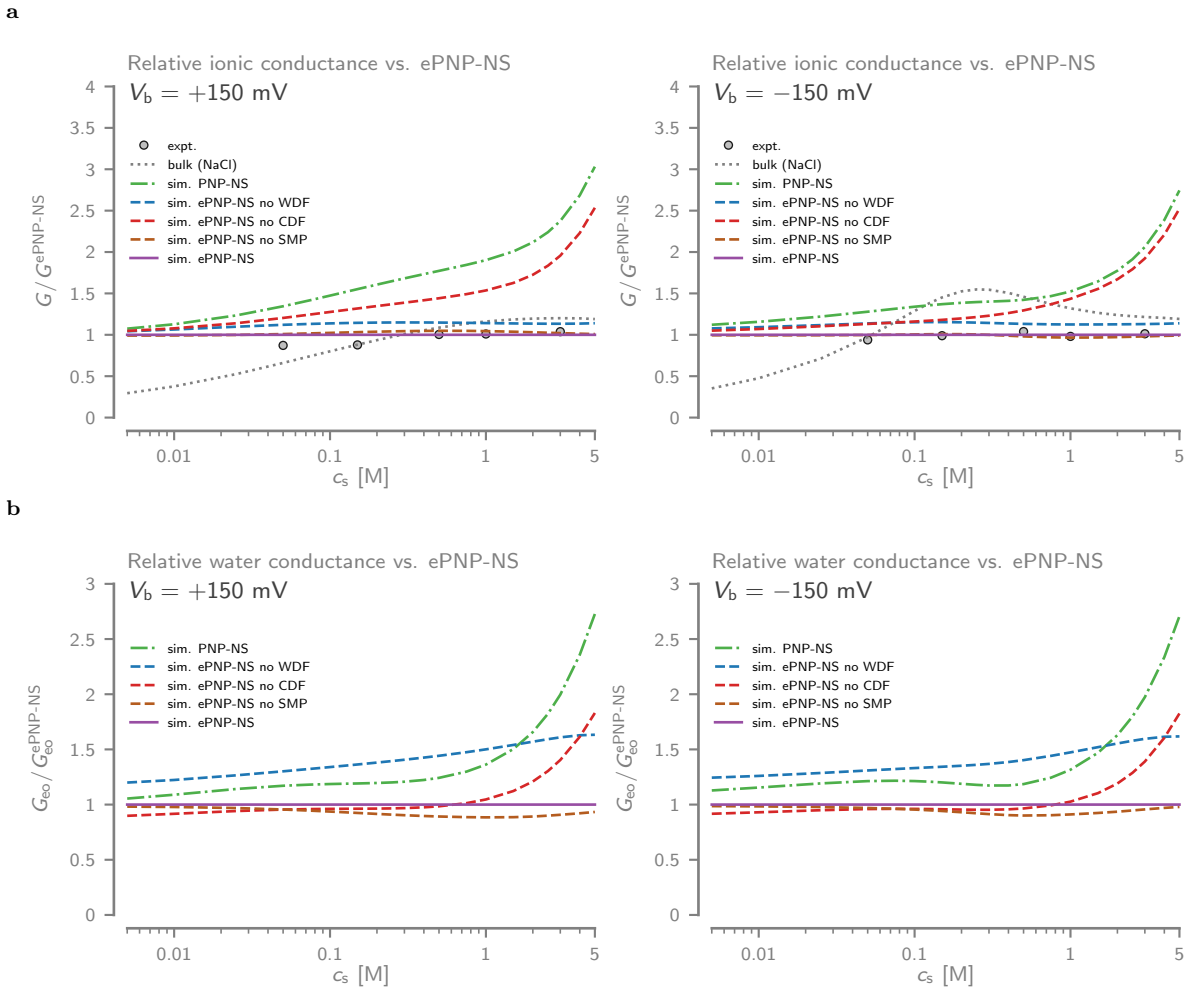

Figure S6. Effect of individual corrections on the simulated ionic and water conductance. (a) The ionic conductance $G = I/V_b$ and (b) the water conductance $G_{eo} = Q_{eo}/V_b$ of ClyA-AS at 150 mV (left) and −150 mV (right), normalized over the values of the ePNP-NS equations. Comparison between the experimental data (expt.), the simple resistor model (bulk, Eq. (S25)), classic PNP-NS (sim. PNP-NS), ePNP-NS without wall distance corrections (sim. ePNP-NS no WDF: $\mathcal{D}_i^w = 1$, $\mu_i^w = 1$, $\eta^w = 1$), ePNP-NS without concentration-dependent corrections (sim. ePNP-NS no CDF: $\varepsilon_{r,f}^c = 1$, $\mathcal{D}_i^c = 1$, $\mu_i^c = 1$, $\eta^c = 1$, $\varrho^c = 1$), ePNP-NS without steric effect (sim. ePNP-NS no SMP: $\boldsymbol{\beta} = 0$) and full ePNP-NS.

curve). By placing an upper limit on the total ion concentration (≈13.3 M in our case), the steric corrections prevent excessive screening of fixed charges by unphysical ionic strengths (*i.e.*, concentrations that would require fitting more ions into a given space than what is physically possible). This is an essential mechanic that allows one to realistically model the electrical double layer near surfaces with high charge densities—as is the case for most biological nanopores.

2.2 Tabulated ion selectivities

Tabulated data on the ion selectivity, in terms of cation transport number t_{Na^+} and cation permeability ratio P_{Na^+} for various salt concentrations and voltages can be found in Tab. S3.

Table S3. Tabulated cation transport numbers and permeability ratios.

	V_b [mV]					
	+150		+100		+50	
c_s [M]	t_{Na^+} [a]	P_{Na^+} [b]	t_{Na^+} [a]	P_{Na^+} [b]	t_{Na^+} [a]	P_{Na^+} [b]
0.005	0.996	235	0.997	313	0.998	410
0.050	0.906	9.62	0.925	12.3	0.941	16.0
0.150	0.786	3.68	0.805	4.13	0.824	4.69
0.500	0.642	1.79	0.649	1.85	0.657	1.91
1.000	0.566	1.30	0.569	1.32	0.572	1.33
2.000	0.502	1.00	0.503	1.01	0.503	1.01
5.000	0.445	0.803	0.445	0.803	0.445	0.803
	V_b [mV]					
	+150		+100		+50	
c_s [M]	t_{Na^+} [a]	P_{Na^+} [b]	t_{Na^+} [a]	P_{Na^+} [b]	t_{Na^+} [a]	P_{Na^+} [b]
0.005	0.998	500	0.998	535	0.998	542
0.050	0.967	29.6	0.966	28.2	0.962	25.1
0.150	0.882	7.51	0.874	6.91	0.860	6.16
0.500	0.687	2.20	0.680	2.12	0.672	2.05
1.000	0.582	1.39	0.579	1.38	0.577	1.36
2.000	0.505	1.02	0.505	1.02	0.504	1.02
5.000	0.445	0.802	0.445	0.802	0.445	0.802

[a] Cation transport number $t_{Na^+} = G_{Na^+}/(G_{Na^+} + G_{Cl^-})$; [b] Cation permeability ratio $P_{Na^+} = G_{Na^+}/(G_{Cl^-})$.

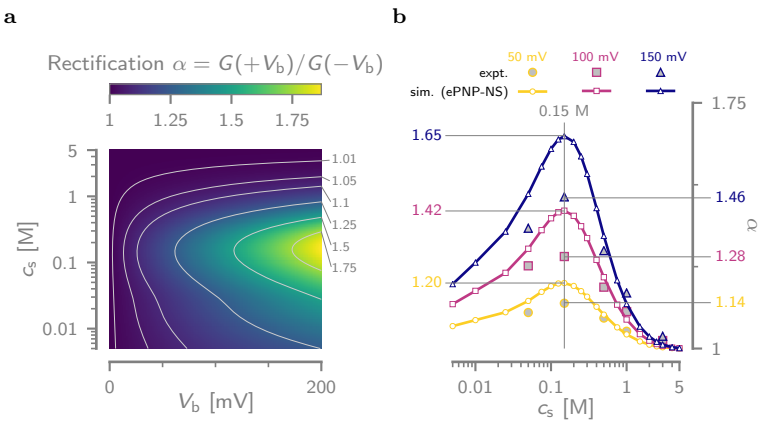

Figure S7. Measured and simulated ionic rectification of single ClyA nanopores. (a) Contourplot of the ionic current rectification $\alpha = G(+V_b)/G(-V_b)$, computed from the ionic conductances in the ePNP-NS simulation, as a function of V_b and c_s. (b) Comparision between the simulated (ePNP-NS) and measured (expt.) α as a function of c_s for 50 mV, 100 mV and 150 mV.

2.3 Ionic current rectification

The ionic current rectification (ICR, α, Fig. S7) represents the relative conductivity of the nanopore at identical, but opposing bias voltages

$$\alpha(V_b) = \frac{G(+V_b)}{G(-V_b)} \text{ , with } V_b \geq 0 \text{ .}$$

Hence, for $\alpha > 0$, the current is higher at positive bias voltages, and vice versa for $\alpha < 0$. The ICR phenomenon results from an asymmetry in the ionic conductance pathways (*e.g.*, moving from *cis* to *trans* is not equivalent as moving from *trans* to *cis*). In turn, this stems from the intrinsic asymmetries of the nanopore itself (*i.e.*, geometry and charge distribution) or its response to the electric field (*i.e.*, gating or electrostriction).

The heatmap of the simulated (ePNP-NS) α (Fig. S7a) reveals that $\alpha > 0$ between 0 mV to 200 mV and 0.005 M to 5 M. It increases monotonically with increasing bias voltage and exhibits a maximum as a function of salt concentration at ≈0.15 M. The concentration dependency of α at 50 mV, 100 mV and 150 mV (Fig. S7b) shows that it increases monotonically with c_s until it reaches a peak value, after which it decreases to approach unity ($\alpha = 1$) at saturating salt concentrations ($c_s \approx 5$ M). Even though the values produced by

the ePNP-NS simulations do not fully match quantitatively to the experimental results, at least for $c_s < 0.5\,\mathrm{M}$, they do (1) reproduce the observed trends qualitatively and (2) exhibit much smaller errors relative to the PNP-NS results (data not shown).

2.4 Peak values of the radial potential profiles inside ClyA

The peak values of the radial electrostatic potential $\langle\varphi\rangle_{\mathrm{rad}}$ at the *cis* entry, middle of the lumen and the *trans* constriction for 0.005 M, 0.05 M, 0.15 M, 0.5 M and 5 M NaCl are summarized in Tab. S4.

Table S4. Peak radial potential.

	$\langle\varphi\rangle_{\mathrm{rad}}$ [mV]		
c_s [M)]	*cis* $z \approx 10\,\mathrm{nm}$	lumen $z \approx 5\,\mathrm{nm}$	*trans* $z \approx 0\,\mathrm{nm}$
0.005	−80	−108	−144
0.05	−34	−50	−86
0.15	−19	−29	−57
0.5	−9.3	−14	−30
5	−1.9	−1.7	−4.2

2.5 Comparison of the *lumen* diameters

A comparison of the ClyA structures equilibrated with molecular dynamics with the crystal (PDBID: 2WCD[24]) and cryo-EM (PDBID: 6MRT[25]) structures can be found in Fig. S8. The molecular surface was colored according to the internal radius r_{int}

$$r_{\mathrm{int},i} = \sqrt{(x_i^2 + y_i^2)} - r_{\mathrm{vdW},i} \tag{S26}$$

with x_i, y_i and $r_{\mathrm{vdW},i}$ the x-coordinate, y-coordinate and van der Waals radius of atom i. All structure were aligned to minimize their RSMD to the initial structure, which has its center of mass at $(0, 0, 55)$.

Our comparison shows that the MD structure does not deviate significantly from the

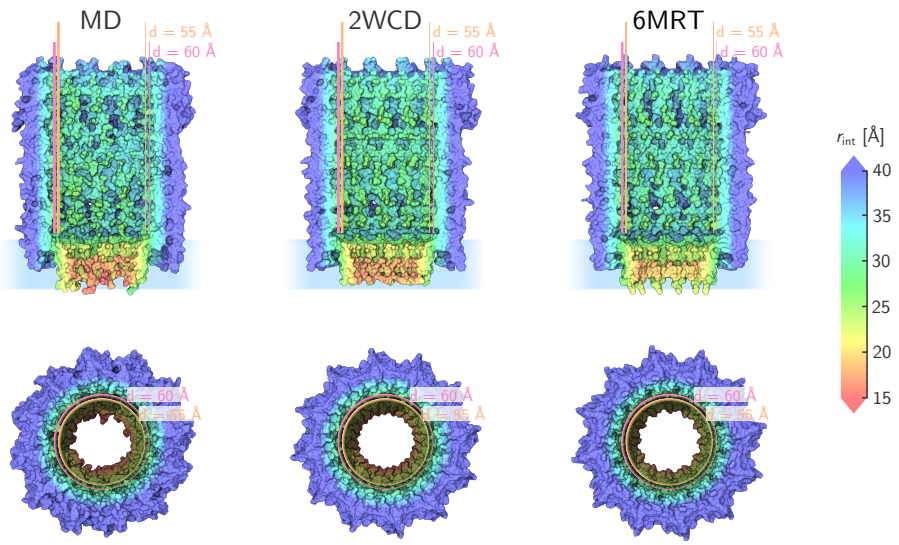

Figure S8. ***Lumen*** **diameters of ClyA.** Side and top view of the molecular surface of the ClyA-AS equilibrated with molecular dynamics (MD, left), with the crystal PDBID: 2WCD [24] (middle) and cryo-EM PDBID: 6MRT [25] (right) structures. Surfaces were colored according to r_{int}, the distance of each atom from the central axis of the pore, reduced with its van der Waals radius (Eq. (S26)). The traditional diameter of 5.5 nm and the 6.0 nm are outlined in orange and pink respectively. Images were rendered using VMD. [26]

crystal and cryo-EM structures in overal geometry. Moreover, the average nanopore diameter in the *cis lumen* is closer to 6 nm than the 5.5 nm reported earlier [27] The value of 5.5 nm should be considered as a measure for the maximum size of a protein that can fit inside dodecameric ClyA without it touching the walls. The 6 nm diameter value given is the average *lumen* diameter, which is slightly larger than 5.5 nm given that it includes—rather than excludes—all corrugations.

2.6 Per-residue B-factors of the molecular dynamics trajectory

Even though the main chain heavy atoms of ClyA were harmonically restrained during the entire MD run, all other atoms were allowed to move freely. This allowed us to sample the conformational landscape of all the ClyA side chains without disrupting the overall structure of the pore and to generate a well-averaged geometry and charge distribution. These thermal

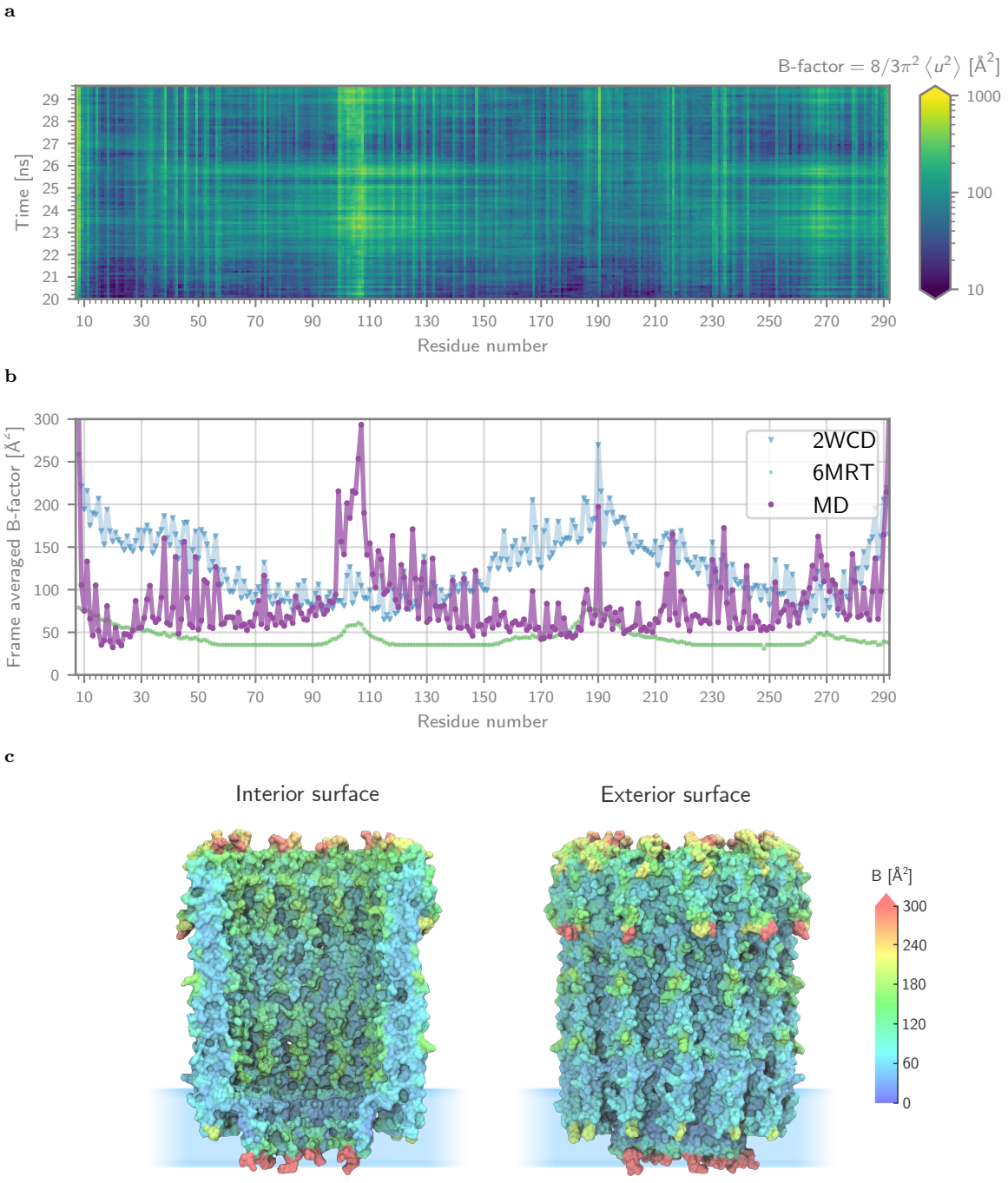

Figure S9. Per-residue B-factors for the last 10 ns of the MD run. (a) Heatmap of the per-residue B-factor (B, Eq. (S27)) of ClyA-AS, averaged over all 12 monomers, as determined by our MD simulation. (b) The data from the heatmap, averaged over all frames and plotted together with the B-factors given by the crystal (PDBID: 2WCD[24] and cryo-EM PDBID: 6MRT[25]) structures of the ClyA dodecamer. (c) Molecular surface plots of the interior (left) and exterior (right) walls of ClyA-AS, colered according to the chain-averaged per-residue B-factor. Images were rendered using VMD.[26]

fluctuations can be quantified with the temperature factor or *B-factor*[28] (B_i)

$$B_i = \frac{8}{3}\pi^2 \left\langle u_i^2 \right\rangle \ , \tag{S27}$$

which can be computed for each atom i from its mean-square displacement (MSD) $\langle u_i^2 \rangle$. Starting from the last 10 ns of our 30 ns MD trajectory, we computed the $\langle u_i^2 \rangle$ using the fast QCP algorithm,[29,30] as implemented in the 'MDAnalysis' Python package.[31] A heatmap of the resulting B-factors for each residue, averaged over all 12 monomers of ClyA, can be found in Fig. S9a. In addition, we plotted the frame-averaged B-factor (Fig. S9b), allowing us to compare the flexibility observed in the MD trajectory with the B-factors given by the dodecamer ClyA crystal (PDBID: 2WCD[24]) and cryo-EM (PDBID: 6MRT[25]) structures. Interestingly, B_i of our MD simulation does not show much agreement with the original 2WCD crystal structure, but it reproduces the more flexible regions observed in the (newer) 6MRT cryo-EM structure (*i.e.*, residue numbers 7 to 20, 95 to 105, 180 to 200 and 260 to 280). Peng and coworkers also started from the 2WCD crystal structure to generate their refined 6MRT model, albeit using a high resolution cryo-EM map as a restraint. Hence, the similarities in flexibility between our model and 6MRT are encouraging that the MD relaxes the structure properly. Finally, we also visualized the the MD B_i on the interior and exterior molecular surface of ClyA-AS (Fig. S9c). This shows that the most flexible regions are the *cis* and *trans* entries of the pore.

References

(1) Soskine, M.; Biesemans, A.; De Maeyer, M.; Maglia, G. Tuning the Size and Properties of ClyA Nanopores Assisted by Directed Evolution. *J. Am. Chem. Soc.* **2013**, *135*, 13456–63.

(2) Newville, M.; Stensitzki, T.; Allen, D. B.; Ingargiola, A. LMFIT: Non-Linear Least-Square Minimization and Curve-Fitting for Python. 2014; `https://zenodo.org/record/11813`.

(3) Mills, R.; Lobo, V. *Self-Diffusion in Electrolyte Solutions: A Critical Examination of Data Compiled from the Literature*; Physical Sciences Data v. 36; Elsevier, 1989.

(4) Esteso, M. A.; Chan, C.-Y.; Spiro, M. Examination of a transference number anomaly: 0.02 mol dm^{-3} aqueous sodium chloride at 25°C. *J. Chem. Soc. Faraday Trans.* **1976**, *72*, 1425.

(5) Haynes, W.; Lide, D.; Bruno, T. CRC Handbook of Chemistry and Physics, 97th edn, Vol. 2016–2017. 2017.

(6) Della Monica, M.; Petrella, G.; Sacco, A.; Bufo, S. Transference Numbers in Concentrated Sodium Chloride Solutions. *Electrochim. Acta* **1979**, *24*, 1013–1017.

(7) Panopoulos, D. K.; Kaneko, H.; Spiro, M. Transference Numbers of Sodium Chloride in Concentrated Aqueous Solutions and Chloride Conductances in Several Concentrated Electrolyte Solutions. *J. Solution Chem.* **1986**, *15*, 243–252.

(8) Schönert, H. Transference Numbers in the H2O + NaCl + MgCl2 System at T = 298.15 K, Determined in a Five-Compartment Hittorf Cell. *J. Solution Chem.* **2013**, *43*, 26–39.

(9) Bianchi, H.; Corti, H. R.; Fernández-Prini, R. The Conductivity of Concentrated Aqueous Mixtures of NaCl and MgCl2 at 25°C. *J. Solution Chem.* **1989**, *18*, 485–491.

(10) Currie, D. J.; Gordon, A. R. Transference Numbers for Cconcentrated Aqueous Sodium Chloride Solutions, and the Ionic Conductances for Potassium and Sodium Chlorides. *J. Phys. Chem.* **1960**, *64*, 1751–1753.

(11) Goldsack, D. E.; Franchetto, R.; Franchetto, A. A. Solvation Effects on the Conductivity of Concentrated Electrolyte Solutions. *Can. J. Chem.* **1976**, *54*, 2953–2966.

(12) Gavish, N.; Promislow, K. Dependence of the Dielectric Constant of Electrolyte Solutions on Ionic Concentration: A Microfield Approach. *Phys. Rev. E* **2016**, *94*, 012611.

(13) Buchner, R.; Hefter, G. T.; May, P. M. Dielectric Relaxation of Aqueous NaCl Solutions. *J. Phys. Chem. A* **1999**, *103*, 1–9.

(14) Hai-Lang, Z.; Shi-Jun, H. Viscosity and Density of Water + Sodium Chloride + Potassium Chloride Solutions at 298.15 K. *J. Chem. Eng. Data* **1996**, *41*, 516–520.

(15) Simakov, N. A.; Kurnikova, M. G. Soft Wall Ion Channel in Continuum Representation with Application to Modeling Ion Currents in α-Hemolysin. *J. Phys. Chem. B* **2010**, *114*, 15180–90.

(16) Makarov, V.; Feig, M.; Andrews, B.; Pettitt, B. Diffusion of Solvent around Biomolecular Solutes: A Molecular Dynamics Simulation Study. *Biophys. J.* **1998**, *75*, 150–158.

(17) Wilson, J.; Sarthak, K.; Si, W.; Gao, L.; Aksimentiev, A. Rapid and Accurate Determination of Nanopore Ionic Current Using a Steric Exclusion Model. *ACS Sensors* **2019**, *4*, 634–644.

(18) Pederson, E. D.; Barbalas, J.; Drown, B. S.; Culbertson, M. J.; Keranen Burden, L. M.; Kasianowicz, J. J.; Burden, D. L. Proximal Capture Dynamics for a Single Biological Nanopore Sensor. *J. Phys. Chem. B* **2015**, *119*, 10448–55.

(19) Rigo, E.; Dong, Z.; Park, J. H.; Kennedy, E.; Hokmabadi, M.; Almonte-Garcia, L.; Ding, L.; Aluru, N.; Timp, G. Measurements of the size and correlations between ions using an electrolytic point contact. *Nat. Commun.* **2019**, *10*.

(20) Pronk, S.; Lindahl, E.; Kasson, P. M. Dynamic Heterogeneity Controls Diffusion and Viscosity Near Biological Interfaces. *Nat. Commun.* **2014**, *5*, 3034.

(21) Lu, B.; Hoogerheide, D. P.; Zhao, Q.; Yu, D. Effective Driving Force Applied on DNA Inside a Solid-State Nnanopore. *Phys. Rev. E* **2012**, *86*, 011921.

(22) Axelsson, O.; He, X.; Neytcheva, M. Numerical Solution of the Time-Dependent Navier–Stokes Eequation for Variable Density–Variable Viscosity. Part I. *Math. Model. Anal.* **2015**, *20*, 232–260.

(23) Kowalczyk, S. W.; Grosberg, A. Y.; Rabin, Y.; Dekker, C. Modeling the Conductance and DNA Blockade of Solid-State Nanopores. *Nanotechnology* **2011**, *22*, 315101.

(24) Mueller, M.; Grauschopf, U.; Maier, T.; Glockshuber, R.; Ban, N. The Structure of a Cytolytic Alpha-Helical Toxin Pore Reveals Its Assembly Mechanism. *Nature* **2009**, *459*, 726–30.

(25) Peng, W.; de Souza Santos, M.; Li, Y.; Tomchick, D. R.; Orth, K. High-resolution cryo-EM structures of the *E. coli* hemolysin ClyA oligomers. *PLOS ONE* **2019**, *14*, e0213423.

(26) Humphrey, W.; Dalke, A.; Schulten, K. VMD: Visual Molecular Dynamics. *J. Mol. Graph.* **1996**, *14*, 33–38.

(27) Willems, K.; Ruić, D.; Biesemans, A.; Galenkamp, N. S.; Dorpe, P. V.; Maglia, G. Engineering and Modeling the Electrophoretic Trapping of a Single Protein Inside a Nanopore. *ACS Nano* **2019**, *13*, 9980–9992.

(28) Bahar, I.; Atilgan, A. R.; Erman, B. Direct evaluation of thermal fluctuations in proteins using a single-parameter harmonic potential. *Fold. Des.* **1997**, *2*, 173–181.

(29) Theobald, D. L. Rapid calculation of RMSDs using a quaternion-based characteristic polynomial. *Acta Crystallogr. A* **2005**, *61*, 478–480.

(30) Liu, P.; Agrafiotis, D. K.; Theobald, D. L. Fast determination of the optimal rotational matrix for macromolecular superpositions. *J. Comput. Chem.* **2009**, n/a–n/a.

(31) Michaud-Agrawal, N.; Denning, E. J.; Woolf, T. B.; Beckstein, O. MDAnalysis: A toolkit for the analysis of molecular dynamics simulations. *J. Comput. Chem.* **2011**, *32*, 2319–2327.